Active millimeter-wave video rate imaging with a staring 120-element microbolometer array*

A. Luukanen[†‡], A. J. Miller, and E. N. Grossman
National Institute of Standards and Technology, Quantum Electrical Metrology Division
325 Broadway, Boulder, CO 80305, U.S.A

ABSTRACT

Passive indoors imaging of weapons concealed under clothing poses a formidable challenge for millimeter-wave imagers due to the sub-picowatt signal levels present in the scene. Moreover, video-rate imaging requires a large number of pixels, which leads to a very complex and expensive front end for the imager. To meet the concealed weapons detection challenge, our approach uses a low cost pulsed-noise source as an illuminator and an array of room-temperature antenna-coupled microbolometers as the detectors. The reflected millimeter-wave power is detected by the bolometers, gated, integrated and amplified by audio-frequency amplifiers, and after digitization, displayed in real time on a PC display. We present recently acquired videos obtained with the 120-element array, and comprehensively describe the performance characteristics of the array in terms of sensitivity, optical efficiency, uniformity and spatial resolution. Our results show that active imaging with antenna-coupled microbolometers can yield imagery comparable to that obtained with systems using MMIC amplifiers but with a cost per pixel that is orders of magnitude lower.

Keywords: Bolometer, array, millimeter-wave, terahertz, concealed weapons, imaging

1. Introduction

This paper describes the results obtained with an active millimeter-wave imaging system incorporating a 120 element focal plane array (FPA) of antenna-coupled microbolometers. The detailed design of the system has been extensively covered in previous proceedings of this conference[1,2,3]. Due to the low signal levels in indoor detection, active illumination is preferable even with tuned RF-receiver based imagers[4]. However, the overall system cost and complexity of high frequency amplifier-based imagers is still too high to be acceptable, while imaging which relies only on total power detection does not benefit from the coherent nature of these devices (with the obvious exception of synthetic aperture techniques). Antenna-coupled microbolometers are extremely simple to fabricate, even in large arrays and have more than adequate sensitivity when used in an active imaging system.

† luukanen@boulder.nist.gov; (303) 497-4590; fax (303) 497-3042
‡ on leave from VTT Information Technology, Espoo, Finland

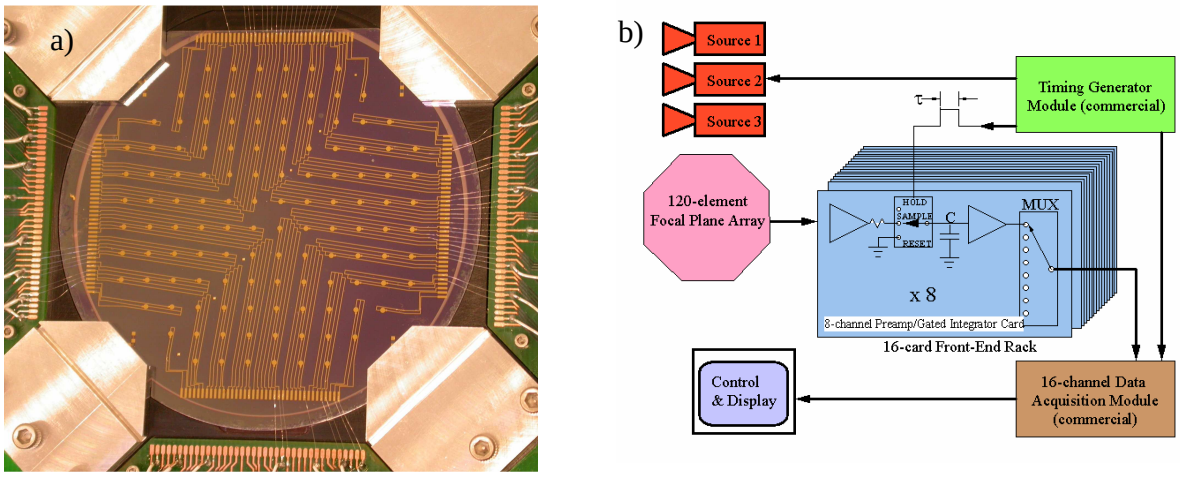

Fig. 1: a) The 120-element antenna-coupled microbolometer focal plane array. The wafer diameter is 75 mm. b) The system architecture. See text for explanation.

The readout of such sensors is essentially a sensitive audio frequency resistance measurement, and the readout electronics can be easily adapted to an application specific integrated circuit (ASIC), shifting the pixel count challenge from integration and interfacing of the FPA to the matching of the FPA pixels with the collecting optics.

2. System description

The imaging system consists of five main parts: the microbolometer focal plane array, three pulsed noise source illuminators operating at 95 GHz, the collecting optics, the readout electronics, and a PC based data acquisition system. The focal plane array (shown in Fig. 1) is fabricated on a 75 mm diameter, high resistivity silicon wafer, and incorporates 120 microbolometers coupled to slot-ring antennas. Fabrication details can be found in Ref. 1. The incident millimeter-wave radiation is coupled to the antenna, and a voltage change proportional to the incident power is produced across the bolometer. The FPA is divided into four quadrants with the DC wiring circuit in each quadrant aligned nearly perpendicular (82°) to the polarization of the pixels in that quadrant. This was done to minimize the coupling between the antennas and the wiring, and to avoid more complex wiring schemes through the substrate. The pixel pitch in the array is 4.75 mm (~1.5 free-space wavelengths). This choice of pitch is based on the 6 mm x 6 mm active area of one pixel determined by prior antenna pattern measurements of a single pixel[5] and measurements on the mutual coupling of pixels in a small array[1]. The illumination of the scene is provided by three 95 (±2.5) GHz IMPATT pulsed noise sources, configured to illuminate the scene from three directions. Illumination from multiple angles is desirable because a reflected signal can be detected regardless of the orientation of typical targets[1].

The peak power of each oscillator pulse is nominally 1 W with a pulse duration of 100 ns that roughly matches the ~200 ns thermal time constant of the bolometers. Eeach source is triggered sequentially at a repetition rate of 83 kHz. The reflected power from the object is then focused onto the FPA by a 30-cm diameter off-axis ellipsoid main aperture located 1.5 m from the object plane. Each pixel in the focal plane is connected via coaxial cabling to the readout electronics. The electronics is divided into 16 amplifier cards, with eight pixels connected to each card. The electronics, which consist of standard audio frequency components, has an equivalent input noise of ~1 $nV/Hz^{1/2}$ and a bandwidth of 5 MHz. Each of the 128 readout channels provides an adjustable DC current bias for the bolometers (typically 3 – 5 mA) and has a preamplification stage, followed by an integrating sample and hold circuit, from which the signal is sent via an analog multiplexer to a commercial 16 channel data acquisition module. The digitized data is then displayed in real time at 30 frames/second on the PC display. The overall power consumption of the entire system is below 250 W, and is dominated by the data acquisition PC. We note that the complete readout electronics rack could be integrated to an ASIC to reduce the package size and lower the power consumption.

3. Focal plane characterization

The architecture of our readout allows for simultaneous characterization of all 120 pixels in terms of their noise and $V(I)$ curve. The $V(I)$ curve provides information on the zero bias resistance R_0 of the devices, the responsivity, and uniformity of the array. To first order, the $V(I)$ curve of a current biased bolometer is given by

$$V = IR_0\left(1+\beta I^2\right), \tag{1}$$

where $\beta = G^{-1}\mathrm{d}R/\mathrm{d}T$ is the specific responsivity for the bolometer with G the thermal conductance between the bolometer and the heat sink. In the FPA pixels, the heat from the pixels escapes through two main routes: laterally to the antenna via G_{ant}, and vertically to the substrate via G_{sub}, with the conduction to the substrate typically dominating. Explicitly, β is given by

$$\beta = \frac{\alpha R_0^2}{G_{sub}R_0 + 12L_0T}, \tag{2}$$

where we have used $\alpha = 1/R_0\mathrm{d}R/\mathrm{d}T$ and the fact that the thermal conductance to the antenna is given by the Wiedemann-Franz law with $G_{ant} = 12L_0T/R_0$ [6]. Here $L_0 = 2.45\cdot10^{-8}\ \mathrm{V^2/K^2}$ is the Lorentz number. The electrical responsivity at current I is given by $S_{elec} = \beta I$. From the FPA $V(I)$ curve measurements, summarized in Fig. 2, we obtained a standard deviation for R_0 of 39 % and 76 % for β. Figure 2 c) shows the scatter plot of $\beta^{1/2}$ against R_0. Because $\beta \propto (R_0/G) \propto w^{-2}$ and $R_0 \propto w^{-1}$, $\mathrm{d}\beta/\beta \propto 2\Delta w/w$ and $\mathrm{d}R_0/R_0 \propto \Delta w/w$. These figures and the scatter plot in Fig. 2 c) indicate that the array non-uniformity is dominated by non-uniformity in the physical linewidth $\Delta w/w$ of the bolometer. The fact that the scatter is mainly in the direction of the theoretical curve shows that the uniformity is limited by the uniformity of our contact lithography. Scatter perpendicular to the fit can be attributed to variations in other factors, such as the film thickness and contact resistance. The dashed line indicates a fit using Eq. (2) with $G_{sub} = 22\ \mu\mathrm{W/K}$ as the fitting parameter. The temperature coefficient of resistance is obtained from prior measurements on our Nb films with $\alpha = 0.2\%/\mathrm{K}$. In the near future we plan to convert to the use of projection photolithography, which will enable us to reduce the line width variation $\Delta w/w$ to about 5 %, thus reducing the scatter in R_0 and β to 5 % and 10 %, respectively.

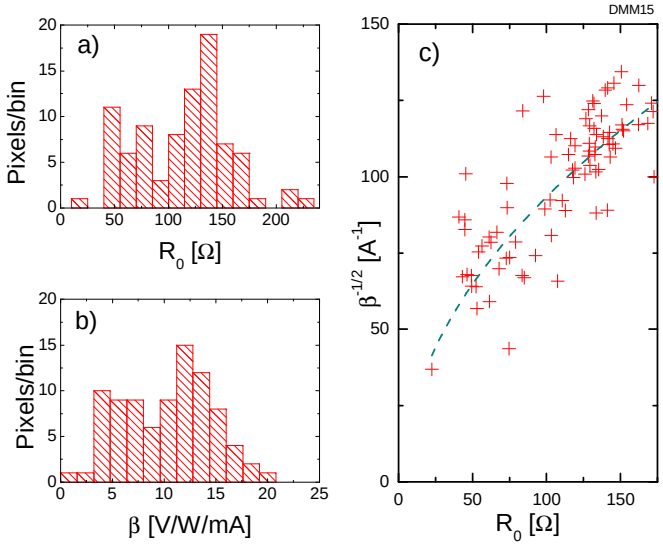

Fig. 2: a) Histogram of zero bias resistances for the FPA. The mean for R_0 is 112 Ω, which implies a nearly perfect match to the (103-45j) Ω ring slot antenna. b) Histogram for the specific responsivities. The mean value for β is 9.5 V/W/mA. c) $\beta^{1/2}$-R_0 scatter plot, together with a fit using Eq. (2).

Overall, the yield of the processing has typically been about 90 %, with dead pixels attributed to either open or short circuits.

4. Optical characterization

The purpose of the optical characterization was to measure the optical coupling efficiency and polarization response for the entire array. This was carried out by placing one of the IMPATT noise sources at a distance of 88 cm from the FPA position, and then measuring the time averaged intensity at the FPA location using a 75 GHz-110 GHz power meter. For the average power we obtained P_{avg}=7.1 μW, which can be turned into intensity by dividing P_{avg} by the 169 mm^2 effective area of the horn. The average power falling on each pixel with a pitch of 4.75 mm is $P_{avg,p}$=7.1 μW/(169 mm^2)·(4.75 mm)^2=950 nW. Next, after placing the FPA at the same location as the power meter, snapshots were acquired for both polarizations using the array. The optical efficiency for each pixel is given by $\eta=S_{opt}/S_{elec}$ where S_{opt} is the optical responsivity. Here some calculation is required to calculate the peak power sensed by the bolometers as the source pulse duration is shorter than the τ_{int}=2.2 μs effective *RC* integration time constant of the integrating sample and hold circuit in the read-out electronics. The voltage pulse entering the electronics is given by $V_{in}(t)=S_{opt}P_{inst}(t)$ where $P_{inst}(t)$ is the instantaneous source power on one pixel. The measured voltage is the output voltage of the gated integrator, given by

$$V_m = \frac{S_{opt}}{\tau_{\text{int}}} \int_0^{\tau_{samp}} P_{inst}(t)dt = \frac{S_{opt}}{\tau_{\text{int}}} \frac{P_{avg,p}}{f_{rep}}, \tag{3}$$

where τ_{samp} is the sampling interval of the sample and hold circuit and f_{rep} is the repetition rate of the noise source. Eq. (3) holds because $\tau_{samp}>>\tau_{bolometer}$, so that the integral is simply the detected energy per pulse. Thus, the optical efficiency for a pixel can be determined from

$$\eta = \frac{S_{opt}}{S_{elec}} = \frac{V_m f_{rep} \tau_{\text{int}}}{P_{avg,p}} \frac{1}{\beta I}. \tag{4}$$

The results for the FPA are shown in Fig. 3 a) for co-polarized radiation. The average efficiency is 6.4 %, which is somewhat lower than the expected ~10 %, based on electromagnetic models for a single pixel. Another unexpected feature in this map is the "X" shaped structure where the efficiency is much higher than the average for the entire FPA. The high efficiency pixels are located at the edge of the quadrants, implying that this effect can be attributed to the coupling between the antennas and the wiring. The pixels that show exceptionally large efficiency in Fig. 3 a) consistently correlate with those with the least amount of wiring in their proximity. In wafers with larger bolometer resistances and thus larger impedance mismatch between the bolometer and the antenna, the "X" appears even more pronounced. Although the optical nonuniformity is larger than expected, this effect can be compensated for by performing a flat field measurement on each wafer with a point source, and use Fig. 3 a) as a gain correction for the FPA pixels.

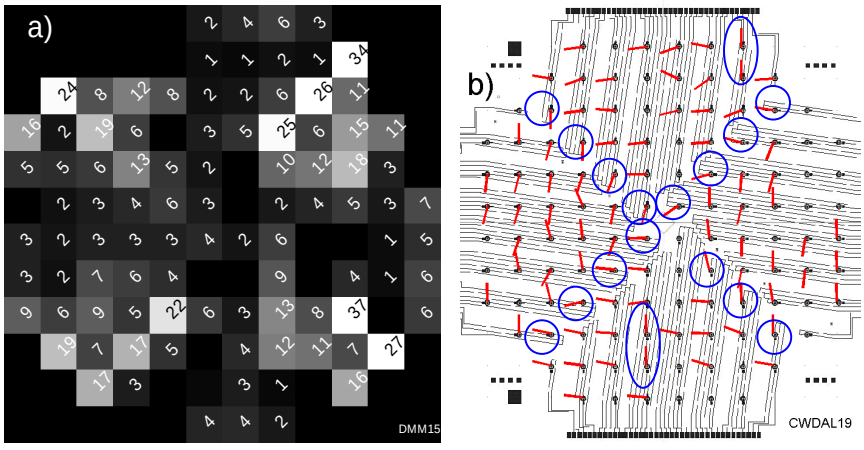

Fig. 3: a) The efficiency map for the array. The numbers correspond to co-polarized efficiency in percents. b) Polarization response of the FPA superimposed on the wiring diagram of the wafer. Pixels marked with a circle show anomalous polarization response.

Nominally, the pixels should be polarizer perpendicular to the wiring connecting to the pixel. Data in a) and b) are from two different FPAs with identical mask designs.

Next, we measured the polarization response of the array. This was carried out by rotating the source polarization over 180 degrees with 1/8 degree increments while acquiring real time data on the array. Figure 3 b) shows the orientation at which the signal of each pixel was maximized. It appears that the anomalously polarized pixels at the end of each quadrant couple with the straight section in the wiring at the end of the particular wiring circuit. It should be noted that these pixels are not same as those showing exceptional coupling efficiency.

5. Imaging results

The imaging system allows us to acquire real time imagery on different objects. The scene is imaged via the main aperture (an off-axis elliptical mirror) with a magnification of 3:1 onto the FPA. Thus, the projected pitch of a pixel at the object plane is 14.25 mm. Because we still only have 120 pixel elements across a field of view of 292 cm^2, the image interpretation is somewhat involved. Augmenting this we use an on-axis video camera for visual reference. First, we imaged a steel ball bearing which should provide us with a triangle of specular reflections from the three sources. The ball bearing has a diameter of 50 mm, corresponding to only 3.5 pixel widths. The locations of the specular reflections are even closer, only 12.5 mm, or 0.9 pixels apart. We can determine the location of each reflection with sub-pixel accuracy by fitting Gaussians to the image and determining the position of the centroids. Figure 4 a) shows a millimeter-wave image of the bearing, with the centroids marked with diamonds. As a reference, Fig. 4 b) is a visible image, taken with the on-axis video camera, with the centroid locations marked with diamonds.

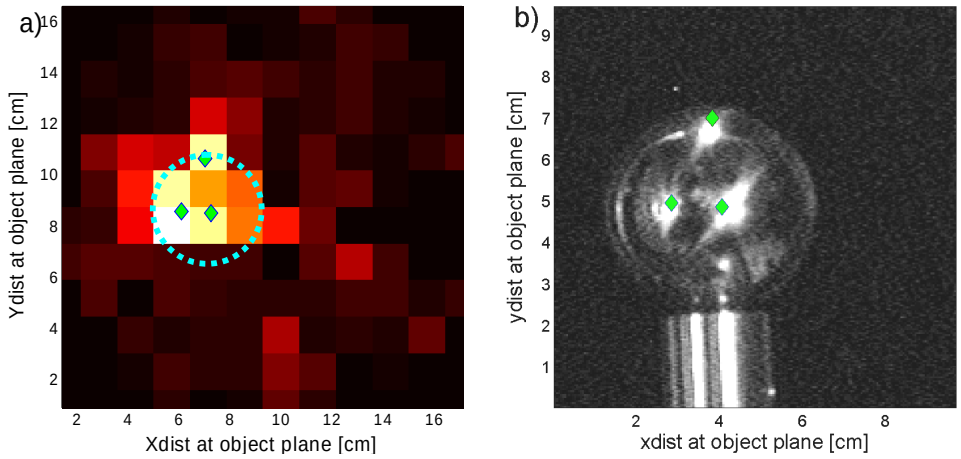

Fig. 4. a) An active mm-wave image of a steel bearing. The Gaussian fit centroids to the image indicate the location of the reflections. The dashed circle indicates the outline of the bearing. b) An optical image of the bearing from the on-axis video camera. Three bright optical reflections indicate the positions of the sources. The diamonds mark the source positions determined from the mm-wave image. Note the slightly different axis for the two figures. The maximum signal level in this image is better than 2000σ; the lit pixels outside the location of the bearing are likely due to audio frequency crosstalk between channels.

Figure 5 shows the imaging results on a more complex object, in this case a pistol. Illumination geometry was identical to that used to acquire Fig. 4. In the figure, the millimeter-wave signals are displayed as contours superimposed on the visible image of the gun. In the linear contour graph, the minimum signal level contour corresponds to a signal level of ~80σ, with σ the noise voltage of the device. Strong returns are seen from the top of the slide where the cartridge ejection port is located, from the trigger assembly as well as from the grip and the safety switch. These hot-spots are consistent with the results obtained with earlier single pixel scanned imagery[1].

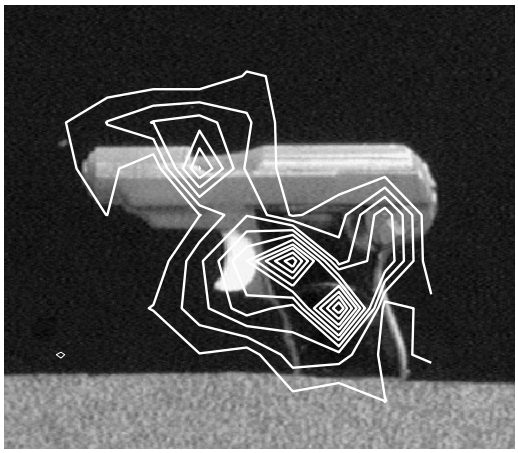

Fig. 5: A visible image of a pistol with superimposed contours of the millimeter-wave image. See text for explanation.

6. Conclusions

We have designed, built and thoroughly characterized a novel millimeter-wave imaging system capable of video rate imagery with 120 fully lithographed pixels. Dedicated data acquisition software allows the real-time observation of millimeter-wave imagery, and an on-axis video camera provides a visible reference that facilitates the image interpretation. The array uniformity is limited by the resolution of our contact photolithography, and further advances are expected in the near future as new devices will be fabricated using projection lithography. The bolometers' noise performance are similar, with an electrical $NEP_{elec} \approx 50$ pW/Hz$^{1/2}$ that is Johnson noise limited.

Further engineering tasks will focus on the reduction of pixel to pixel cross talk, that we attribute to the coupling of the three trigger signals to the readout channels. Slow drifts in the channels will be removed by providing an intermittent dark frame at a frequency above the $1/f$ noise knee of the system. Recently, we started the construction of a new imager[7], in which the 120 pixels will be configured to a linear array, and combined with conical scanning optics that can scale the pixel count fairly easily to 38,400. The linear array will also likely provide much higher coupling efficiency as the wiring is connected from the side to each pixel and there are no large number of on-wafer wires present. Further improvement of the bolometers' NEP is expected with recently developed air-bridge microbolometers[8,9], with projected electrical NEPs approaching 1 pW/Hz$^{1/2}$.

In the long term, we see the possibility of constructing truly staring focal plane arrays with dedicated integrated readout circuitry integrated in the same package as the bolometer FPA. In conclusion, we feel that the antenna-coupled microbolometer active imaging technology can provide high quality millimeter-wave videos with a fraction of the systems cost associated with RF amplification based technologies.

ACKNOWLEDGEMENTS

We are grateful to Kathleen Higgins and Nick Paulter of the Office of Law Enforcement Standards for originally starting this program, under Natl. Inst. of Justice sponsorship.

REFERENCES

[1] E.N. Grossman and A.J. Miller, "Active millimeter-wave imaging for concealed weapons detection", *Proc. SPIE* **5077**, pp.62-70 (2003).

[2] N.G. Paulter, E.N. Grossman, G.N. Stenbakken, B.C. Waltrip, S. Nolen, and C.D. Reintsema, "Design of an active mm-wave concealed object imaging system", *Proc. SPIE* **4373**, pp.64-71 (2001).

[3] E.N. Grossman, S. Nolen, N.G. Paulter and C.D. Reintsema, "Concealed weapons detection system using uncooled, pulsed, imaging arrays of millimeter-wave bolometers", *Proc. SPIE* **4373**, pp.7-15 (2001).

[4] P.R. Coward and R. Appleby, "Development of an illumination chamber for indoor millimeter-wave imaging", *Proc. SPIE* **5077**, pp.54-61 (2003).

[5] S. Nolen, T.E. Harvey, C.D. Reintsema and E.N. Grossman, "Properties of cavity-backed slot-ring antennas at 95 GHz", *Proc. SPIE* **4373**, pp.49-57 (2001).

[6] Neikirk, D.P., Lam, W.W., and Rutledge, D.B., "Far-infrared Microbolometer Detectors", *Int. J. of Ir and Mm-Waves*, **5**(3), p. 245-277 (1984).

[7] E.N. Grossman, A. Luukanen and A.J. Miller, "Terahertz active direct detection imagers", these proceedings.

[8] A. Luukanen and J.P. Pekola, "A superconducting antenna-coupled hot-spot microbolometer", *Appl. Phys. Lett.* **82**, pp.3970-3972 (2003)

[9] A.J. Miller, A. Luukanen , and E.N. Grossman, "Micromachined antenna-coupled uncooled microbolometers for terahertz imaging arrays", these proceedings.